Biowaste-derived substances as a tool for obtaining magnet-sensitive materials for environmental applications in wastewater treatments

Biowaste-derived substances as a tool for obtaining magnet-sensitive materials for environmental applications in wastewater treatments

Flavia Franzoso[a], Roberto Nisticò[a,*], Federico Cesano[a,b], Ingrid Corazzari[a,b,c], Francesco Turci[a,b,c], Domenica Scarano[a,b], Alessandra Bianco Prevot[a], Giuliana Magnacca[a,b], Luciano Carlos[d], Daniel O. Mártire[e].

[a] University of Torino, Department of Chemistry, [b] NIS Interdepartmental Centre, and [c] "G. Scansetti" Interdepartmental Centre for Studies on Asbestos and other Toxic Particulates, Via P. Giuria 7, 10125 Torino, Italy

[d] Instituto de Investigación y Desarrollo en Ingeniería de Procesos, Biotecnología y Energías Alternativas, PROBIEN (CONICET-UNCo), Buenos Aires 1400, Neuquén, Argentina

[e] Instituto de Investigaciones Fisicoquímicas Teóricas y Aplicadas (INIFTA), Universidad Nacional de La Plata, Casilla de Correo 16, Sucursal 4, (1900) La Plata, Argentina

* Corresponding author. E-mail: roberto.nistico@unito.it, Ph.: +39-011-6707533, Fax: +39-011-6707855

Abstract

In this study, bio-based substances (BBS) obtained from composted urban biowaste are used as stabilizers for the synthesis of magnet-sensitive nanoparticles (NPs). The BBS-stabilized NPs are characterized by means of different techniques (FTIR, XRD, SEM, BET analysis, magnetization curves). Additionally, TGA coupled on-line with FTIR and GC/MS analysis of the exhausted gas are performed in order to simultaneously identify all the degradation products and evaluate the exact composition of such BBS-stabilized materials. Moreover, Fenton-like or photo-Fenton-like experiments carried out at circumneutral pH are performed in order to evaluate the BBS-functionalized NPs photo-activity towards the degradation of caffeine (taken as model emerging pollutant). The obtained promising results encourage the use of BBS as a green alternative tool for the preparation of smart materials with enhanced magnet-sensitive properties, also suitable for applications in wastewater purification treatments.

Keywords: Biomasses valorization; Emerging pollutants; Iron oxides; Magnetic materials; Fenton and Photo-Fenton reactions.

1. Introduction

Together with the human technological expansion, there is a significant increasing of the anthropogenic impact on water sources, thus creating a dramatic reduction of the available resources [1]. In fact, even though the primary renewable source of fresh water is the continental rainfall, which generates a global supply of 40000-45000 km^3 per year, this is not enough to fulfill the increasing demand caused by human population growing [2]. Besides this, one of the major problems related to fresh water quality is represented by pollutants contamination, difficult to remove by the traditional treatments [3-4]. Among the more classic pollutants, a wide group of anthropic chemical substances named emerging pollutants (EPs), whose dangerousness is only recently recognized but not yet regulated by environmental laws, is receiving great attention from the scientific community (i.e. human pharmaceuticals and veterinary medicines, nanomaterials, personal-care products, paints and coatings) [5-7].

In order to solve this issue, many studies focused on innovative wastewater treatments are being carried out currently, for instance the exploitation of no-cost bio-based sources (i.e. microalgae, biomasses and humic/fulvic acids, chitosan and its derivatives, etc.) as novel adsorbents/active species for the removal of EPs which is very promising allowing both economic and environmental benefits [8-12].

At the same time, advanced oxidation processes (AOPs) have been widely studied as a green alternative treatment for the purification of contaminated water [13-18]: Fenton and photo-Fenton reactions (induced by Fe(II)/H_2O_2 species without or with UV irradiation respectively) are widely studied and utilized to promote the degradation of organic contaminants through the action of highly oxidizing species, mainly hydroxyl radicals ($^{\bullet}OH$), generated *in situ* from H_2O_2 decomposition catalyzed by Fe(II)-sources and accelerated by UV-Vis irradiation ($\lambda < 500$ nm, in

the photo-Fenton process) [19]. Photo-Fenton processes are applied in treating several industrial wastewaters, such as dye industry [20], pesticides [21], phenols and organic compounds [22-23], and real contaminated effluents [24]. Additionally, as reported by Bauer et al [25], photo-Fenton treatments are the cheapest one among the other available AOPs. Quite recently, several efforts were realized by worldwide experts to enhance the efficiency/feasibility of both Fenton and photo-Fenton processes by testing different materials [26-27], as well as different AOPs methods [28-29]. In particular, most of the problems related to the industrial scale up of such processes are both the pH correction and the reactants consumption [30-32], thus the possibility of using low-cost easily-removable materials working at circumneutral pH is extremely promising. As evidenced in the literature, the introduction of humic-like substances in both Fenton and photo-Fenton processes seems to significantly favor the pollutant degradation capacity in aqueous environment at circumneutral pH, even though the effective role played by humic-like substances in the oxidation mechanism is still not fully solved [6,8,33-34]. As reported in several studies, humic substances directly improve the degradation of organic pollutants under UV-Vis irradiation in two different ways: either involving the triplet-excited states of the O-containing functionalities present in the humic-like structures [35], or through the formation of many reactive O-containing species, such as hydroxyl radicals, singlet oxygen ($^1O_2(a^1\Delta_g)$), and superoxide species [6,36-37]. Additionally, humic and humic-like substances not only favor the direct oxidation of organic pollutants, but also speed up the iron redox reactions Fe(II)/Fe(III), thus accelerating both Fenton and photo-Fenton mechanisms [38-39].

In this respect, it appears very convenient to use a combined approach to remove the organic contaminants in water applying bio-based substances together with an iron-source. Quite recently, magnetite (Fe(II)/Fe(III) mixed valence oxide), maghemite (γ-Fe_2O_3), and hematite (α-Fe_2O_3) have been successfully verified as alternative sources of iron in heterogeneous AOPs [40-41]. If the iron source is magnetite or another magnet-sensitive material, it becomes also possible to recover the species active in the removal of contaminants from aqueous matrices after the treatment.

Magnetic materials are usually synthesized by coprecipitation method in basic medium (between 8 and 14) [40]. Respect to the stoichiometric ratio, a slight excess of Fe(II) in the synthesis is preferred to prevent the possible oxidation of Fe(II) atoms with formation of maghemite as impurity since the reaction mixture was exposed to the air. According to the literature [42], for Fe(III)/Fe(II) < 1.75 pure magnetite NPs are obtained, whereas for Fe(III)/Fe(II) ≥ 1.75 the final product consists of a mixture of magnetite and maghemite. Additionally, since magnetite is sensitive to oxidation, maghemite can be easily formed by topotactic oxidation of magnetite due to aging phenomena [43-44]. In order to avoid the complete oxidation of magnetite/maghemite phases to hematite, the stabilization with an organic coating is usually carried out [43,45-46]. In general, the addition of chelating anions (i.e. carboxylate or hydroxyl-carboxylate species) or polymeric complexing agents (such as chitosan, dextran, starch, or polyvinyl alcohol) during the formation/precipitation of magnetite can both drive the nanoparticles size-control as well as enhance the iron oxide stability (in particular, preserving magnetite from oxidation). Also biomasses and residual biowaste-derived substances have been considered as source of organic coating [40] valorizing urban and/or agricultural biowastes into added-value chemicals (thus re-entering them into the economic cycle) [47].

Therefore, the aim of this study is the use of Bio-Based Substances obtained from Green Compost (BBS-GC) as synthesis intermediates/stabilizers for the production of BBS-covered magnetite nanoparticles. Such BBS are lignin-derived supramolecular aggregates with a very complex structure similar to humic-like substances (namely, aromatic and aliphatic chains functionalized with acid and basic functional groups whose chemical structure is fully reported in **Table S1**). Three different synthesis formulations were investigated.

The application of such BBS-coated magnet-sensitive nanoparticles was investigated in heterogeneous Fenton-like and photo-Fenton-like processes for wastewater treatments, taking caffeine (a stimulating agent) as model EPs.

2. Experimental

2.1 Materials

Magnetite precursors were anhydrous ferric chloride $FeCl_3$ (CAS 7705-08-0, purity ≥ 98%, Fluka Chemika) and ferrous sulphate heptahydrate $FeSO_4 \cdot 7H_2O$ (CAS 7782-63-0, purity ≥ 99.5%, Fluka Chemika). Bio-Based Substances (BBS-GC) were isolated from composted urban biowastes (urban public park trimming and home gardening residues) aged for more than 180 days, obtained from the *ACEA Pinerolese Industriale S.p.A*. waste treatment plant located in Pinerolo (Italy). Other reagents used were: ammonium hydroxide solution (CAS 1336-21-6, NH_3 essay 28-30%, E. Merck), caffeine ($C_8H_{10}N_4O_2$, CAS 58-08-2, purity ≥ 99.0%, Sigma-Aldrich), hydrogen peroxide (H_2O_2, CAS 7722-84-1, essay 31%, Anedra Research AG), methanol HPLC grade (CH_3OH, CAS 67-56-1, essay 99.8%, Sintorgan), phosphoric acid (H_3PO_4, CAS 7664-38-2, essay 84-86%, Cicarelli Laboratorios), 1,10-phenanthroline (*o*-phenanthroline, $C_{12}H_8N_2$, CAS 66-71-7, purity ≥ 99.0%, Sigma-Aldrich), and ammonium phosphate ($NH_4H_2PO_4$, CAS 7722-76-1, essay ≥ 99.0, Sigma-Aldrich). All aqueous solutions for HPLC analysis were prepared using ultrapure water Millipore Milli-Q™. All chemicals were used without further purification.

2.2 Preparation of magnetite/BBS nanoparticles

BBS-stabilized magnetite nanoparticles were synthesized following a modified procedure already reported in the literature [40,43]. In detail, 3.7 g of $FeCl_3$ and 4.17 g of $FeSO_4 \cdot 7H_2O$ (molar ratio Fe(III)/Fe(II) = 1.5) were dissolved in 100 mL of deionized water and heated up to 90°C. Once the target temperature was reached, two solutions were added simultaneously: a) 10 mL of 25 vol.% ammonium hydroxide, and b) 50 mL of a previously prepared BBS aqueous solution. In particular, three BBS-containing solutions with different content of BBS were employed: 1, 2, and 3 wt.%, respectively. The final mixture was mechanically stirred at isothermal conditions (90°C) for 30 min and then cooled down to room temperature (RT). In this way a dispersion of BBS-stabilized magnetic iron oxide nanoparticles has been directly obtained in a one-step process by co-precipitation method. Such dark-brown solutions were: i) purified by washing twice with deionized

water, ii) deposited onto glass Petri dishes, and iii) oven-dried at 80°C overnight. The resulting magnetic materials were manually crumbled. Depending on the different wt.% of BBS (namely 1 wt.%, 2 wt.% and 3 wt.%), the obtained nanoparticles were coded with the acronym MB1, MB2 and MB3, respectively). Non-stabilized magnetite (M0), obtained from the already described procedure without BBS addition, was taken as neat magnetite reference.

2.3 Physicochemical characterizations

Scanning electron microscopy (SEM) analyses were carried out by using a ZEISS EVO 50 XVP microscope with LaB_6 source, equipped with detectors for secondary electron collection. SEM micrographs were performed after sputtering the samples with a gold layer (ca. 10 nm thickness, Bal-tec SCD050 sputter coater). Additionally, the particles size distribution was evaluated on SEM micrographs at 150000× magnification by using the software Particule2 (version 2.0) and calculating the diameter size on 500 nanoparticles. The nanoparticles diameter values are corrected with respect to the gold coating thickness.

Magnetization measurements were carried out with a LakeShore 7404 vibrating sample magnetometer. The hysteresis loop of the samples was registered at RT and the magnetic field was cycled between -20000 and 20000 Gauss.

N_2 adsorption-desorption experiments were carried out by using an ASAP 2020 instrument (Micromeritics) in order to determine the specific surface area (BET model) [48] and porosity (BJH model) of all samples [49]. Samples (ca. 0.5 g) were previously outgassed at 70°C for about 24 h in vacuum (residual pressure 10^{-2} mbar) to ensure the complete removal of atmospheric contaminants from their surface before the analysis.

Fourier transform infrared (FTIR) spectra were recorded in transmission mode by means of a Bruker Vector 22 spectrophotometer equipped with Globar source, DTGS detector, and working with 128 scans at 4 cm^{-1} resolution in the 4000-400 cm^{-1} range. Samples were dispersed in KBr (1:20 weight ratio).

X-ray diffraction (XRD) patterns were obtained by means of an X'Pert PRO MPD diffractometer from PANalytical, equipped with Cu anode, working at 45 kV and 40 mA, in a Bragg-Brentano geometry performing experiments on flat sample-holder configurations. The acquisition was performed in a 0.02° interval steps, with 45 s $step^{-1}$ to obtain a good signal to noise ratio. The magnetite particles size was also estimated by means of the Scherrer equation (**Equation 1**):

$$\tau = \frac{K\lambda}{\beta \cos \theta}$$

where τ is the mean size of the crystalline domains (expressed in nm), K is a shape factor (typical value adopted is 0.9), λ is the X-ray wavelength (0.154 nm), β is the line broadening at half the maximum intensity (FWHM) of the selected Bragg angle after subtracting the instrumental line broadening (expressed in radians), and θ is the Bragg angle (expressed in radians). For the magnetite NPs size quantification, the Bragg angle selected is the magnetite reflection (311) at ca. 2θ = 35.6°.

Colorimetric quantification of free-Fe(II) was performed using a double-beam T90+ UV-Vis spectrometer (PG Instruments Ltd), in a quartz cuvette, slow speed mode at 1 nm resolution in the 200-800 nm range. The conventional colorimetric tests were performed by mixing ca. 10 mg of each sample with *o*-phenanthroline and acetate buffer (pH = 4) forming the orange-red ferrous-tris-*o*-phenanthroline complex [50]. The free-Fe(II) was quantified after 60 minutes of contact.

Thermo-gravimetric analyses (TGA) were carried out by means of an ultra-microbalance (sensitivity 0.1 μg) connected with both a time-resolved FTIR and a GC/MS detectors. Samples in powdery form (ca. 30 mg) were placed into an open platinum pan and heated from 30 to 900°C at the heating rate of 10°C min^{-1} under dynamic nitrogen atmosphere (gas purity: 99.9995%; flow rate: 35 mL min^{-1}) by using a Perkin-Elmer Pyris 1 TGA instrument (Waltham, MA, USA). The exhausted gas (gas flow 65 mL min^{-1}) was piped via a pressurized heated transfer line (Redshift S.r.l., Vicenza, Italy) and analyzed continuously by the FTIR detector (Spectrum 100, Perkin-Elmer), equipped with a thermostated conventional gas cell. Temperature/time-resolved spectra

were acquired in the 4000-600 cm^{-1} wavenumber range with a 0.4 cm^{-1} resolution and analyzed with the Spectrum software (Perkin-Elmer). Temperature-resolved infrared profiles of each single species desorbed from the analyzed samples were obtained measuring the intensity of a representative peak of the investigated species at a selected wavenumber. The Ɛ values were obtained employing "PPM/Meter Gas Cell Concentration Data" from Specac (Orpington, UK) which was obtained by measuring the gases in a one meter path-length gas cell at 25°C at 1 atmosphere pressure with a nitrogen gas mix. The absorbance value given for the concentration of gas was expected at the indicated wavenumber position (i.e. 2360 cm^{-1} due to the asymmetric stretching mode of CO_2 and 960 cm^{-1} due to the symmetric bending mode of NH_3). The absorbance reported was 0.40 a.u. for CO_2 (100 ppm), and 0.12 a.u. for NH_3 (100 ppm). On the basis of these data, we calculated the absorption coefficients (namely $ƐCO_2 = 4.0\ 10^{-3}$ ppm^{-1} m^{-1}, and $ƐNH_3 = 1.2\ 10^{-3}$ ppm^{-1} m^{-1}) by applying the Lambert-Beer's law. In our experimental determinations, the maximum intensity point due to the asymmetric stretching mode of CO_2 was recorded at 2359 cm^{-1}, while the maximum intensity point due to the symmetric bending mode of NH_3 occurred at 965 cm^{-1} [51].

2.4 Fenton-like and photo-Fenton-like degradation of caffeine

Degradation experiments were performed: i) for Fenton-like tests, in a closed Pyrex-flask (containing 200 mL solution at RT) covered with an aluminum paper (i.e. in the dark) under continuous magnetic stirring, or ii) for photo-Fenton-like tests, in a cylindrical Quartz vessel (diameter: 5 mm, containing 200 mL solution, at 32.5±2.5°C) under continuous magnetic stirring. Experiments were performed in two replicas and the average profiles were reported. The initial concentration of the caffeine was 5 mg L^{-1}. Experiments were performed by addition of 100 mg of NPs (neat magnetite or BBS-stabilized samples) in presence of hydrogen peroxide (H_2O_2, 0.4 mM). The amount of hydrogen peroxide added was chosen considering half the stoichiometric concentration which is enough to reach an efficient caffeine degradation, as suggested in the literature [52]. To verify the natural photolysis of caffeine, experiments in presence of only H_2O_2

were also performed. The effect of the hydroxyl radicals was evaluated performing experiments in presence of the BBS-stabilized NPs and in absence of H_2O_2, whereas in order to evaluate the importance of the magnetite-core in the NPs, control experiments in homogeneous phase (i.e., 100 mg of BBS and 0.4 mM H_2O_2) were also realized. The possible effect of free-Fe(II) release was evaluated by performing experiments in absence of NPs and by addition of Fe(II) at the concentration quantified for MB2 by colorimetric tests. Finally, the effect of UV irradiation was checked performing Fenton experiments in the dark. Reactions were run at the pH=6, which did not change during experiments. A photochemical reactor (Rayonet RPR-100) equipped with 8 RPR-3500 A lamps with emission centered at 350 nm was used as irradiation source (for photo-Fenton tests). The incident photon rate (3.50×10^{-5} Einstein L^{-1} s^{-1}) was measured using a potassium ferrioxalate actinometer (see **Figure S1**). During each experiment, 3 mL sample aliquots were periodically collected at fixed time from the flask/vessel. Before analysis, aliquots were magnet-cleaned (in order to avoid the presence of the magnetic nanoparticles) and filtered through nylon membranes with 0.45 μm cut-off.

The caffeine concentration was determined by means of high pressure liquid chromatography (HPLC), using a Hewlett-Packard TI series 1050 HPLC system with auto-sampler and multi-wavelength detection, equipped with a Inertsil ODS-3 column (4.6 mm × 250 mm, spherical particles size 5 μm in size, modified with end-capped octadecyl groups, pH ranging in the 2.0-7.5 interval). The eluent was a 1% H_3PO_4 in 50/50 (vol.%) methanol/water mixture at 0.8 mL min^{-1} constant flux. The injection volume was 50 μL with a re-equilibration time of 10 min. The caffeine detection wavelength was 275 nm.

UV-Visible spectra of caffeine solution before and after degradation were recorded by means of a double-beam T90+ UV-Vis spectrometer (PG Instruments Ltd) with slow speed at 1 nm resolution in the 200-800 nm range.

3. Results and Discussion

3.1 Morphological, physicochemical and magnetic characterization

Nitrogen sorption measurements were performed on both pure magnetite and BBS-stabilized samples, and results are summarized in **Table 1**. All the isotherms (not reported for the sake of brevity) show a profile IV, with a hysteresis loop of type H3 (according to the IUPAC classification) in the relative pressure range 0.4-1. The BET surface area of the reference magnetite (M0) is 77 m^2g^{-1}, whereas all BBS-stabilized samples present a very low specific surface area and mesopores volume, ranging values from 4 m^2g^{-1} (MB1) up to 33 m^2g^{-1} (MB3). This particular behavior clearly confirmed that the presence of BBS dramatically influences both the aggregation and the porosity in the final material (*vide infra* for the sample composition).

Infrared spectra of both reference materials (neat magnetite M0 and neat BBS) and MB2 (MB1 and MB3 are not shown for the sake of brevity) are collected in **Figure 1**. In particular, the presence of BBS in MB2 is mainly confirmed by the carboxylate stretching mode at ca. 1600 cm^{-1}. The band at 1120 cm^{-1} is typical of C-O stretching mode of organic matter (i.e. polysaccharides and other BBS-derived substances) adsorbed onto the iron oxide surface. Magnetite phase is clearly evidenced by signals at 575 and 620 cm^{-1} due to Fe-O stretching vibrations. Significant differences were observed by comparing the FTIR spectra in the region relative to carboxylic/carboxylate functionalities [40] evidencing the interaction between BBS-carboxylate anions and the iron oxide surface. As already evidenced by Ou and coworkers [53] for humic substances, in all BBS-stabilized NPs it was observed the formation of a very sharp band at 1400 cm^{-1} associated with the carboxylate-iron bond stretching. Other signals in the range 900-700 cm^{-1} not evidenced in the figure are due to ammonium-containing salts, which are byproducts of the co-precipitation reaction.

X-ray diffraction (XRD) patterns were used to identify the iron oxide phases presented in all samples (**Figure 2**). Even in this case, only the MB2 sample was discussed, since similar results were obtained for the other BBS-stabilized samples. All the crystalline planes reflection registered for MB2 sample at 2θ = 30.1° (220), 35.4° (311), 43.0° (400), 53.9° (422) 57.2° (511), and 62.6° (440) are consistent with the presence of magnetite phase (reference code 00-019-0629, ICCD

Database) [44]. The signals not related to magnetite phase (main relevant one at 2θ = 33°) are consistent with the presence of ammonium-containing salts, namely ammonium chloride (reference code 01-073-0363, ICCD Database), confirming the FTIR results.

In order to estimate the average particle size, Scherrer formula applied to the (311) magnetite signal was used (see **Table 1**). The size of the crystalline domains related to magnetite phase are not homogeneous (all the signals are quite broad) and a slight decrease in the calculated average NPs size was observed in the BBS-stabilized samples from MB1 to MB3. In particular, it is possible to note that the size of the crystalline domains decreases increasing the BBS concentration. A possible explanation of this behavior can be found in the action developed by BBS in the synthesis. It is added to the reaction mixture just after the beginning of the coprecipitation reaction (i.e. right after the formation of the crystal seeds) and it covers the crystals avoiding their agglomeration. If the amount of biosurfactant is high, its presence not only avoids the agglomeration of the particles but also limits the growth of the crystals which remain small.

The morphology of all BBS magnet-sensitive NPs, dispersed in water and deposited on sample holder, was evaluated by means of SEM (TEM image of MB1 is reported in [40]). Considering the similarity shown by the samples, only MB2 images are reported in **Figure 3**. In detail, MB2 material appeared as aggregates of roughly spherical particles (see **Figure 3A**) whose size distribution is reported in **Figure 3B**. MB2 particles show diameters in the range 16-55 nm, with the 40% of the particles centered between 26 and 30 nm. These values are in very good agreement with those calculated from Scherrer equation for the same sample (i.e. 22 ± 6 nm), also considering that Scherrer calculation considers only the magnetite crystalline core without taking into account the organic coating around the particles.

Considering the magnetic behaviors, all BBS-stabilized samples are easily recoverable from their aqueous dispersions through the action of a permanent magnet. Moreover, dried BBS-stabilized materials do not lose their magnetic properties for at least one year, due to the BBS protective coating. Magnetization curves collected at RT of all samples are resumed in **Figure 4**. Basing on

the results obtained, all samples exhibit superparamagnetic behaviors, with almost zero remanence (Mr) and very low coercitivity (Hc below 10 G). The saturation magnetization (Ms) of all BBS-stabilized magnet-sensitive NPs were 53 (MB1), 36 (MB2), and 30 (MB3) emu g^{-1}, respectively. The decrease in Ms for all the samples compared to the reference magnetite M0 (64 emu g^{-1}) is due to the presence of the organic coating as well as to a different average size of magnetic domains (**Table 1**). According to the literature, the presence of a coating agent decreases the materials uniformity due to quenching phenomena of surface moments, thus inducing a reduction of magnetic moments in the nanoparticles [40,54]. Moreover, the decrease of the Ms as decreasing the particle size is due to the increasing of the surface spin canting due to increasing disorder of the adsorbed species as the particles decrease in size [55].

3.2 Thermal stability and BBS degradation profiles

Neat BBS and BBS-stabilized nanoparticles thermal behaviors were analyzed by TGA in the temperature range 30-900°C under flow of N_2 in order to establish the thermal stability of the samples and to determine the BBS amount in the hybrid materials. NH_3 and CO_2 evolved during the heating ramp were continuously monitored by the FTIR detector coupled to the gravimetric apparatus. FTIR profiles of the evolved species, expressed as ppm/mg of sample, were determined relating the IR absorbance measured at a specific wavenumber (i.e. 965 cm^{-1} for NH_3 and 2359 cm^{-1} for CO_2) to their concentration according to the Lambert-Beer law relationship employing the spectra of each species at a known concentration from the instrument database. In **Figure 5** are reported both the weight loss % and its derivative curve (panel A), together with the FTIR profiles (panel B) of NH_3 and CO_2 evolved during the heating of MB2. These data were compared to those obtained with pure BBS at the same experimental conditions. TGA analysis of BBS presented two main weight losses: the first one was due to moisture content (water evaporation), as highlighted by the minimum at ca. 100°C on the derivative curve, whereas the second one, which occurred between 250 and 600°C, was principally due to the degradation of the BBS-organic matter, but also the presence of inorganic contributions need to be considered. A carbonaceous residue (containing

some inorganic ashes), which represented ca. the 50% of the starting sample, was collected in the pan after the heating ramp.

The thermal degradation of MB2 shows three main degradation steps evidenced by the three minima on the derivative curve at ca. 230, 310 and 430°C, due to degradation of both ammonium-containing salts (as byproducts of the synthesis, according to FTIR and XRD analyses) and BBS coating. In addition, in the temperature range between 700 and 900°C an important weight loss was recorded and attributed to the chemical reduction of magnetite into wüstite (FeO) under the adopted reducing conditions (nitrogen flux) [43].

During the heating ramp, the evolution of NH_3 and CO_2 species released from the sample was monitored by FTIR detector. It is evinced that the evolution of CO_2 from neat BBS takes place via a two-step process since two maxima are evidenced in the CO_2 release curve, whereas the same experiment carried out with MB2 evidenced that CO_2, which reasonably comes from the decarboxylation of the BBS organic component, is released through a single broad step. The release of NH_3 from BBS is attributed to the decomposition of both N-containing functionalities and ammonium-containing ashes (ash content: 31.2 wt.%, see the **Table S1**). Also, the rather high amount of NH_3 released at lower temperature (150-400°C) by MB2 sample should be due to the decomposition of ammonium-containing synthesis byproducts (in accordance to FTIR and XRD analyses). Analogue results have been obtained with both MB1 and MB3 (data not shown for brevity).

The percentage composition of materials (in terms of BBS, ashes, ammonium-containing salts and magnetite) was quantified by the following procedure:

i. Integrating the FTIR profile in the temperature range 200-600°C (for CO_2) and 150-800 (for NH_3). The starting temperature chosen for CO_2 integration corresponds to the first degradation step.

ii. Calculating the (BBS+ashes) wt.% in each MB sample on the basis of the CO_2 released, normalized to the CO_2 released by neat BBS.

iii. According to **Table S1,** the ashes content in BBS is 31.2 wt.% and thus the real BBS organic fraction forming the stabilizing coating was assumed to be complementary (i.e. the 68.8 wt.% of the BBS+ashes fraction).

iv. Estimating the byproduct content in this way: a) the difference of the total [NH_3] released from each material and the theoretical [NH_3] due to the (BBS+ashes) fraction in the sample was calculated, b) such [NH_3] difference was expressed as ammonium-salts wt.% as a proportion respect to the total [NH_3] released by the reference NH_4^+-containing salt (i.e. $NH_4H_2PO_4$).

v. Finally the residual wt. % was assigned to the iron oxide fraction in the sample.

The results obtained are summarized in **Table 2**. Since the amount of volatile products released by the samples is proportional to the composition of the material, we can estimate the relative content of BBS and magnetite in the hybrids.

The results evidenced that the increase of BBS concentration in the synthesis produces a decrease of the BBS loading in the obtained material. And this behavior is also sustained by the BET surface area variation and the average magnetite size calculated by Scherrer formula. This odd result can actually be explained considering that BBS in aqueous solution tends to organize in supramolecular arrays in a micellization process, due to its amphiphilic properties, and this probably affects the loading capacities [8,12,56].

The content of byproducts (NH_4^+-containing salts, quantified by volatile NH_3 species expressed as amount of $NH_4H_2PO_4$) confirms the FTIR and XRD results, since the samples purity increases by decreasing the concentration of BBS in the starting solution (namely MB1>MB2>MB3).

To further clarify the mechanism of the organic substrate thermal degradation, the gas evolved during the BBS pyrolysis via TGA at the temperature corresponding to the maximum speed of the degradative process (i.e. 350°C) was analyzed by GC/MS. This experimental approach was chosen to unveil the presence of volatile organic specie which might be produced as intermediate during

the pyrolysis. The GC/MS analysis did not evidence the release of organic molecule (data not reported for brevity) indicating that the pyrolysis of the BBS organic structure induces the formation only of small molecules (including CO_2 and NH_3) mainly due to BBS functional groups loss, thus leaving a carbonaceous residue, very promising for the production of carbon-based materials.

3.3 The magnetite/BBS photo-activity in Fenton and photo-Fenton conditions

Preliminary experiments were performed in order to evaluate the potential application of BBS-stabilized magnetite nanoparticles towards the degradation of caffeine (reference EP) at the natural pH (ca. 5-6) in Fenton-like and photo-Fenton-like processes. Upon UV irradiation in the presence of H_2O_2 (**Figure 6A**) or BBS/H_2O_2, no significant degradation of caffeine was observed (**Figure 6B**, top). Such results allow to hypothesize that in the adopted experimental conditions, there is neither efficient generation of $^{\bullet}OH$ by H_2O_2 photolysis nor relevant production of reactive species by BBS photoactivation. The presence of neat magnetite and H_2O_2 slightly favored the degradation of caffeine (87% of residual caffeine after 60 min, as reported in **Figure 6A**) in agreement with the literature data [41].

On the contrary, the addition of BBS-stabilized magnetic NPs in the presence of H_2O_2 dramatically changes the degradation behavior, evidencing different efficiency depending on the initial BBS concentration used to prepare the different NPs. In particular (**Figure 6A**), the caffeine degradation profile observed in the presence of MB1 is comparable to the one observed when using neat M0. MB2 promotes the almost complete caffeine degradation after 60 minutes under UV irradiation (5% of residual caffeine after 60 min), as demonstrated by the UV-Vis spectra of caffeine solution reported in **Figure 6C**; the performance of MB3 is lower (60% of residual caffeine after 60 min). In order to give a rationale for the observed behavior, data reported in Table 2 could give a help: the less efficient NPs (MB1) contains the relative highest amount of BBS and the lowest magnetite amount; MB2 and MB3 contain a comparable magnetite amount, while MB2 has higher BBS content. Several previous studies dealing with the use of magnetite-based materials in

Fenton/photo-Fenton-like processes (see [57] and references therein), reported that the efficiency of the photo-Fenton-like process with magnetite depends greatly on the dissolution of iron from the solid and the oxidation proceeds mostly via homogeneous Fenton. Moreover, the presence of chelating agents (e.g. EDTA, oxalate, tartrate, citrate) facilitates the dissolution of iron from the solid, thanks to the formation of iron complexes, thus favoring the homogeneous reaction. In the present case BBS contain carboxylic and phenolic group able to form iron complexes thus favoring the iron dissolution and the occurrence of photo-Fenton-like process. At the same time it can be hypothesized that, above a certain concentration, the scavenging of reactive species by BBS becomes relevant; such a behavior has been already discussed for BBS in homogeneous system [58-59]. Based on this, MB2 composition could represent the best compromise among several different operating mechanisms; nevertheless being the system highly complicated and several equilibria involved, further research is needed.

Based on the observed performance we focused our attention on MB2 sample for further experiments.

The capacity of MB2 in caffeine degradation was also evaluated under UV irradiation in the absence of H_2O_2 (**Figure 6B**, bottom). In this case, the caffeine degradation was negligible, thus confirming the importance of H_2O_2 for the degradation process and further supporting the hypothesis of a photo-Fenton-like process, as main mechanism, excluding adsorption phenomena. Some experiments were therefore performed to assess the role of UV irradiation (i.e. in the dark, **Figure 6D**). The results obtained evidence that the MB2 activity toward caffeine degradation in the absence of UV irradiation is significantly lower (ca. 65% of residual caffeine after 60 min).

In order to evaluate the relevance of homogeneous degradation process due to the possible presence of free-Fe(II) in solution, a colorimetric test with *o*-phenantroline has been performed and results are reported in **Table S2** (calibration curve is reported in **Figure S2**). It is evident that a not negligible amount of Fe(II) is released in solution (0.001 g L^{-1}), thus allowing a homogeneous Fenton or photo-Fenton reactions to occur, justifying the caffeine degradation. In any case, the

amount of Fe(II) released (with respect to the amount of sample) is similar for each sample under study, therefore the free-Fe(II) presence should not be the only factor favoring the caffeine degradation. Some experiments were then performed in the presence of Fe(II) (taking $FeSO_4 \cdot 7H_2O$ as a source of Fe(II)) at the same concentration of iron leached from MB2 (i.e. 0.001 g L^{-1}, corresponding to 0.28% w/w of the magnetite content in MB2 in suspension) under both Fenton and photo-Fenton conditions at weak acid pH (ca. 6). Results evidence that the degradation of caffeine in presence of Fe(II) without BBS is significantly lower if compared to the same experiments performed in presence of MB2 material. In particular, in the presence of Fe(II) no relevant degradation is observed in Fenton conditions and ca. 70% of abatement is registered after 60 min in photo-Fenton condition (MB2 sample caused 30% of abatement after 60 min in the dark and 95% in photochemical treatment), thus confirming the importance of BBS in the caffeine abatement. It could be hypothesized that the chelating groups present in BBS structure allow to stabilize iron species in solution, avoiding their conversion in the corresponding hydroxides. At the same time, the magnetite, stabilized by BBS, could be considered as an iron "reservoir" for the Fenton and photo-Fenton processes.

Actually, the effective role of BBS in the degradation process is still not fully understood, nevertheless BBS molecules seem to play as acceleration agent for the caffeine degradation, under both Fenton and photo-Fenton conditions. Moreover, BBS allow to carry out Fenton-based treatments (usually performed at very low pH) in mild conditions (i.e. pH=6), and this fact represents a relevant advance in wastewater treatments.

Some indications concerning the stability of BBS in homogeneous systems can be obtained from the literature [60], suggesting the possibility of reusing these materials in several cycles of reaction.

4. Conclusions

In conclusion, BBS (humic-like biopolymers derived from composted urban biowaste) have been proven to be effective stabilizing agent for the low-cost synthesis of magnet-sensitive nanoparticles, produced via co-precipitation method. Magnet-responsive NPs compared with other systems used

for Fenton and photo-Fenton processes show the advantage of being easily recoverable from the reaction media using an external magnetic field.

Different amounts of BBS in the synthesis procedure has been investigated and a deep physicochemical characterization of such BBS-coated magnet-sensitive samples have been performed.

All samples are made of roughly spherical nanoparticles, which give rise to the formation of some aggregates with very low specific surface area and mesopores volume.

Magnetic properties showed that, even if the BBS coating decreases the saturation magnetization values (Ms) with respect to the neat magnetite, such BBS-coated materials are still highly magnet-sensitive and can be easily separated from their aqueous dispersions. Additionally, the natural oxidation involving the interconversion of magnetite into hematite is overcome due to the BBS preserving role. Magnetite stability was maintained for more than one year.

In wastewater treatment, even though it is still not fully-assessed the effective role of BBS, Fenton-like and photo-Fenton-like experiments highlight the peculiar capacity of BBS in promoting the caffeine degradation. The BBS-stabilized samples can be effective even at circumneutral pH in the presence of H_2O_2, upon UV irradiation.

These preliminary tests evidence how BBS can be used as a promising green actor in wastewater purification treatments.

5. Acknowledgements

This work was realized with the financial support for academic interchange by the Marie Sklodowska-Curie Research and Innovation Staff Exchange project funded by the European Commission H2020-MSCA-RISE-2014 within the framework of the research project Mat4treaT (Project number: 645551). Compagnia di San Paolo and University of Torino are gratefully acknowledged for funding Project Torino_call2014_L2_126 through ‘‘Bando per il finanziamento di progetti di ricerca di Ateneo – anno 2014’’ (Project acronym: Microbusters). The TGA-FTIR-

GCMS measures have been obtained with the equipment acquired by the "G. Scansetti" Interdepartmental Center for Studies on Asbestos and Other Toxic Particulates thanks to a grant by the Compagnia di San Paolo, Torino, Italy. Additionally, authors would like to acknowledge Dr. Flavio R. Sives (La Plata, Argentina) for magnetization measurements, together with Dr. Janina A. Rosso and Ms. Francisca Aparicio (La Plata, Argentina) for their precious help.

References

[1] B.W. Atkinson, F. Bux, H.C. Kasan, Considerations for applications of biosorption technology to remediate metal-contaminated industrial effluents, **Water SA**, 1998, 24, 129-135.

[2] A.K. Kivaisi, The potential for constructed wetlands for wastewater treatment and reuse in developing countries: A review, **Ecological Engineering**, 2001, 16, 545-560.

[3] S.D. Richardson, T.A. Ternes, Water analysis: Emerging contaminants and current issues, **Analytical Chemistry**, 2014, 86, 2813-2848.

[4] L. Demarchis, M. Minella, R. Nisticò, V. Maurino, C. Minero, D. Vione, Photo-Fenton reaction in the presence of morphologically controlled hematite as iron source, **Journal of Photochemistry and Photobiology A: Chemistry**, 2015, 307, 99-107.

[5] B. Petrie, R. Barden, B. Kasprzyk-Hordern, A review on emerging contaminants in wastewaters and the environment: Current knowledge, understudied areas and recommendations for future monitoring, **Water SA**, 2015, 72, 3-27.

[6] N. Klamerth, S. Malato, M.I. Maldonado, A. Agüera, A. Fernández-Alba, Modified photo-Fenton for degradation of emerging contaminants in municipal wastewater effluents, **Catalysis Today,** 2011, 161, 241-246.

[7] A.B.A. Boxall, *New and Emerging Water Pollutants arising from Agriculture*, OECD Publishing, 2012. http://www.oecd.org/tad/sustainable-agriculture/49848768.pdf.

[8] G. Magnacca, E. Laurenti, M.C. González, A. Arques, A. Bianco Prevot, Effect of humic substances and bioorganic substrates from urban wastes in nanostructured materials applications

and synthesis, In: A. Arques, A. Bianco Prevot (Eds.), *Soluble Bio-based Substances Isolated from Urban Wastes. Environmental Applications*, Springer International Publishing AG, Cham (Switzerland), 2015, pp. 41-58.

[9] B. De Benedetti, A.C. Barbera, P. Freni, P. Tecchio, Wastewater valorization adopting the microalgae accelerated growth, **Desalination and Water Treatment**, 2015, 53, 1001-1011.

[10] W.S. Wan Ngah, L.C. Teong, M.A.K.M. Hanafiah, Adsorption of dyes and heavy metal ions by chitosan composites: A review, **Carbohydrate Polymers**, 2011, 83, 1446-1456.

[11] G. Magnacca, E. Laurenti, E. Vigna, F. Franzoso, L. Tomasso, E. Montoneri, V. Boffa, Refuse derived bio-organics and immobilized soybean peroxidase for green chemical technology, **Process Biochemistry,** 2012, 47, 2025-2031.

[12] R. Nisticò, M. Barrasso, G.A. Carrillo Le Roux, M.M. Seckler, W. Sousa, M. Malandrino, G. Magnacca, Biopolymers from composted biowaste as stabilizers for the green synthesis of spherical and homogeneously sized silver nanoparticles for textile application on natural fibers, **ChemPhysChem,** 2015, 16, 3902-3909.

[13] A.G. Trovó, T.F.S. Silva, O. Gomes Jr., A.E.H. Machado, W. Borges Neto, P.S. Muller Jr., D. Daniel, Degradation of caffeine by photo-Fenton process: Optimization of treatment conditions using experimental design, **Chemosphere**, 2013, 90, 170-175.

[14] N. Klamerth, S. Malato, M.I. Maldonado, A. Aguera, A.R. Fernández-Alba, Application of photo-Fenton as a tertiary treatment of emerging contaminants in municipal wastewater, **Environmental Science and Technology**, 2010, 44, 1792-1798.

[15] N. Klamerth, L. Rizzo, S. Malato, M.I. Maldonado, A. Aguera, A.R. Fernández-Alba, Degradation of fifteen emerging contaminants at μg L^{-1} initial concentrations by mild solar photo-Fenton in MWTP effluents, **Water Research**, 2010, 44, 545-554.

[16] C. Sirtori, A. Zapata, I. Oller, W. Gernjak, A. Agüera, S. Malato, Decontamination industrial pharmaceutical wastewater combining solar photo-Fenton and biological treatment, **Water Research**, 2009, 43, 661-668.

[17] A. Zapata, I. Oller, L. Rizzo, S. Hilgert, M.I. Maldonado, J.A. Sánches-Pérez, S. Malato, Evaluation of operating parameters involved in solar photo-Fenton treatment of wastewater: interdependence of initial pollutant concentration, temperature and iron concentration, **Applied Catalysis B**, 2010, 97, 292-298.

[18] A. Bernabeu, S. Palacios, R. Vicente, R.F. Vercher, S. Malato, A. Arques, A.M. Amat, Solar photo-Fenton at mild conditions to treat a mixture of six emerging pollutants, **Chemical Engineering Journal**, 2012, 198-199, 65-72.

[19] A. Babuponnusami, K. Muthukumar, A review on Fenton and improvements to the Fenton process for wastewater treatment, **Journal of Environmental Chemical Engineering**, 2014, 2, 557-572.

[20] J. Feng, X. Hu, P.L. Yue, H.Y. Zhu, G.Q. Lu, Degradation of azo-dye Orange II by a photoassisted Fenton reaction using a novel composite of iron oxide and silicate nanoparticles as a catalyst, **Industrial & Engineering Chemistry Research**, 2003, 42, 2058–2066.

[21] H. Fallmann, T. Krutzler, R. Bauer, S. Malato, J. Blanco, Applicability of the photo-Fenton method for treating water containing pesticides, **Catalysis Today**, 1999, 54, 309-319.

[22] L. Yu, J. Chen, Z. Liang, W. Xu, L. Chen, D. Ye, Degradation of phenol using Fe_3O_4-GO nanocomposite as a heterogeneous photo-Fenton catalyst, **Separation and Purification Technology**, 2016, 171, 80-87.

[23] S. Giannakis, M.I. Polo López, D. Spuhler, J.A. Sánchez Pérez, P. Fernández Ibáñez, C. Pulgarin, Solar disinfection is an augmentable, in situ-generated photo-Fenton reaction-Part 2: A review of the applications for drinking water and wastewater disinfection, **Applied Catalysis B: Environmental**, 2016, 198, 431-446.

[24] S. Miralles-Cuevas, I. Oller, A. Agüera, J.A. Sánchez Pérez, S. Malato, Strategies for reducing cost by using solar photo-Fenton treatment combined with nanofiltration to remove microcontaminats in real municipal effluents: Toxicity and economic assessment, **Chemical Engineering Journal**, 2016, in press.

[25] R. Bauer, H. Fallmann, The photo-Fenton oxidation — A cheap and efficient wastewater treatment method, **Research on Chemicals Intermediates**, 1997, 23, 341-354.

[26] B. Bethi, S.H. Sonawane, B.A. Bhanvase, S.P. Gumfekar, Nanomaterials-based advanced oxidation processes for wastewater treatment: A review, **Chemical Engineering and Processing**, 2016, 109, 178-189.

[27] S. Lacombe, T. Pigot, Materials for selective photo-oxygenation vs. photocatalysis: preparation, properties and applications in environmental and health fields, **Catalysis Science and Technology**, 2016, 6, 1571-1592.

[28] S. Gligorovski, R. Strekowski, S. Barbati, D. Vione, Environmental implications of hydroxyl radicals (˙OH), **Chemical Reviews**, 2015, 115, 13051-13092.

[29] A. Babuponnusamia, K. Muthukumar, Advanced oxidation of phenol: A comparison between Fenton, electro-Fenton, sono-electro-Fenton and photo-electro-Fenton processes, **Chemical Engineering Journal**, 2012, 183, 1-9.

[30] S. Miralles-Cuevas, I. Oller, A. Agüera, J. A. Sánchez Pérez, R. Sánchez-Moreno, S. Malato, Is the combination of nanofiltration membranes and AOPs for removing microcontaminants cost effective in real municipal wastewater effluents?, **Environmental Science: Water Research & Technology**, 2016, 2, 511-520.

[31] T.F.C.V. Silva, A. Fonseca, I. Saraiva, R.A.R. Boaventura, V.J.P. Vilar, Scale-up and cost analysis of a photo-Fenton system for sanitary landfill leachate treatment, **Chemical Engineering Journal**, 2016, 283, 76-88.

[32] A. Buthiyappan, A.A.A. Raman, W.M.A.W.Daud, Development of an advanced chemical oxidation wastewater treatment system for the batik industry in Malaysia, **RSC Advances**, 2016, 6, 25222-25241.

[33] J. Gomis, R.F. Vercher, A.M. Amat, D.O. Mártire, M.C. González, A. Bianco Prevot, E. Montoneri, A. Arques, L. Carlos, Application of soluble bio-organic substances (SBO) as

photocatalysts for wastewater treatment: Sensitizing effect and photo-Fenton-like process, **Catalysis Today**, 2013, 209, 176-180.

[34] J. Gomis, L. Carlos, A. Bianco Prevot, A.C.S.C. Teixeira, M. Mora, A.M. Amat, R. Vicente, A. Arques, Bio-based substances from urban waste as auxiliaries for solar photo-Fenton treatment under mild conditions: Optimization of operational variables, **Catalysis Today**, 2015, 240A, 39-45.

[35] S. Canonica, Oxidation of aquatic organic contaminants induced by excited triplet states, **Chimia**, 2007, 61, 641-644.

[36] P.P. Vaughan, N.V. Blough, Photochemical formation of hydroxyl radical by constituents of natural waters, **Environmental Science and Technology**, 1998, 32, 2947-2953.

[37] A. Paul, S. Hackbarth, R.D. Vogt, B. Röder, B.K. Burnison, C.E.W. Steinberg, Photogeneration of singlet oxygen by humic substances: comparison of humic substances of aquatic and terrestrial origin, **Photochemical and Photobiological Sciences**, 2004, 3, 273-280.

[38] M. Moonshine, Y. Rudich, S. Katsman, E. R. Graber, Atmospheric HULIS enhance pollutant degradation by promoting the dark Fenton reaction, **Geophysical Research Letters**, 2008, 25, L20807.

[39] B.M. Voelker, B. Sulzberger, Effects of fulvic acid on Fe(II) oxidation by hydrogen peroxide, **Environmental Science and Technology**, 1996, 30, 1106-1114.

[40] G. Magnacca, A. Allera, E. Montoneri, L. Celi, D.E. Benito, L.G. Gagliardi, M.C. González, D.O. Mártire, L. Carlos, Novel magnetite nanoparticles coated with waste-sourced biobased substances as sustainable and renewable adsorbing materials, **ACS Sustainable Chemistry and Engineering,** 2014, 2, 1518-1524.

[41] M. Minella, G. Marchetti, E. De Laurentiis, M. Malandrino,V. Maurino, C. Minero, D. Vione, K. Hanna, Photo-Fenton oxidation of phenol with magnetite as iron source, **Applied Catalysis B: Environmental**, 2014, 154-155, 102-109.

[42] W. Jiang, K.-L. Lai, H. Hu, X-B. Zeng, F. Lang, K.-X. Liu, Y. Wu, Z.-W. Gu, The effect of $[Fe^{3+}]/[Fe^{2+}]$ molar ratio and iron salts concentration on the properties of superparamagnetic iron

oxide nanoparticles in the water/ethanol/toluene system, **Journal of Nanoparticle Research**, 2011, 13, 5135-5145.

[43] F. Cesano, G. Fenoglio, L. Carlos, R. Nisticò, One-step synthesis of magnetic chitosan polymer composite films, **Applied Surface Science,** 2015, 345, 175-181.

[44] R.M. Cornell, U. Schwertmann, *The Iron Oxides: Structure, Properties, Reactions, Occurrences and Uses*, Wiley-VCH, Weinheim, Germany, 2003.

[45] Y. Li, D. Yuan, M. Dong, Z. Chai, G. Fu, Facile and green synthesis of core-shell structured magnetic chitosan submicrospheres and their surface functionalization, **Langmuir,** 2013, 29,11770-11778.

[46] T. Nardi, M. Sangermano, Y. Leterrier, P. Allia, P. Tiberto, J.-A.E. Månson, UV-cured transparent magnetic polymer nanocomposites, **Polymer,** 2013, 54, 4472-4479.

[47] C. Briens, J. Piskorz, F. Berruti, Biomass valorization for fuel and chemicals production – A review, **International Journal of Chemical Reactor Engineering,** 2008, 6, DOI:10.2202/1542-6580.1674.

[48] S. Brunauer, P.H. Emmett, E. Teller, Adsorption of gases in multimolecular layers, **Journal of the American Chemical Society**, 1938, 60, 309-319.

[49] E.P. Barrett, L.G. Joyner, P.P. Halenda, The determination of pore volume and area distributions in porous substances. I. Computations from nitrogen isotherms, **Journal of the American Chemical Society**, 1951, 73, 373-380.

[50] W.B. Fortune, M.G. Mellon, Determination of iron with *o*-phenanthroline: A spectrophotometric study, **Industrial & Engineering Chemistry Analytical Edition**, 1938, 10, 60-64.

[51] I. Corazzari, R. Nisticò, F. Turci, M.G. Faga, F. Franzoso, S. Tabasso, G. Magnacca, Advanced physico-chemical characterization of chitosan by means of TGA coupled on-line with FTIR and GCMS: Thermal degradation and water adsorption capacity, **Polymer Degradation and Stability**, 2015, 112, 1-9.

[52] M. Munoz, Z.M. de Pedro, J.A. Casas, J.J. Rodriguez, Assessment of the generation of chlorinated byproducts upon Fenton-like oxidation of chlorophenols at different conditions, **Journal of Hazardous Materials**, 2011, 190, 993–1000.

[53] X. Ou, S. Chen, X. Quan, H. Zhao, Photochemical activity and characterization of the complex of humic acids with iron(III), **Journal of Geochemical Exploration**, 2009, 102, 49-55.

[54] D.K. Kim, M. Mikhaylova, Y. Zhang, M. Muhammed, Protective coating of superparamagnetic iron oxide nanoparticles, **Chemistry of Materials**, 2003, 15, 1617-1627.

[55] E.D. Smolensky, H.-Y.E. Park, Y. Zhou, G.A. Rolla, M. Marjańska,M. Botta, V.C. Pierre, Scaling laws at the nano size: The effect of particle size and shape on the magnetism and relaxivity of iron oxide nanoparticle contrast agents, **Journal of Materials Chemistry B**, 2013, 1, 2818-2828.

[56] P. Savarino, E. Montoneri, S. Bottigliengo, V. Boffa, T. Guizzetti, D.G. Perrone, R. Mendichi, Biosurfactants from urban wastes as auxiliaries for textile dyeing, **Industrial & Engineering Chemistry Research**, 2009, 48, 3738-3748.

[57] M. Munoz, Z.M. de Pedro, J.A. Casas, J.J. Rodriguez, Preparation of magnetite-based catalysts and their application in heterogeneous Fenton oxidation – A review, **Applied Catalysis B**, 2015, 176–177, 249–265.

[58] P. Avetta, F. Bella, A. Bianco Prevot, E. Laurenti, E. Montoneri, A. Arques, L. Carlos, Waste cleaning waste: photodegradation of monochlorophenols in the presence of waste derived organic catalysts, **ACS Sustainable Chemistry & Engineering**, 2013, 1, 1545–1550.

[59] J. Gomis, A. Bianco Prevot, E. Montoneri, M.C. Gonzalez, A.M. Amat, D.O. Martire, A. Arques, L. Carlos, Waste sourced bio-based substances for solar-driven wastewater remediation: Photodegradation of emerging pollutants, **Chemical Engineering Journal**, 2014, 235, 236-243.

[60] J. Gomis, M.G. Gonçalves, R.F. Vercher, M.C. Sabater, M.A. Castillo, A. Bianco Prevot, A.M. Amat, A. Arques. Determination of photostability, biocompatibility and efficiency as photo-Fenton auxiliaries of three different types of soluble bio-based substances (SBO), **Catalysis Today**, 2015, 252, 177–183.

Captions to Figures

Table 1. BET surface areas, BJH pore volumes and magnetite NPs size estimated by Scherrer equation applied on the XRD (311) magnetite main reflection.

Table 2. Evolved volatile species measured by TGA-FTIR analysis and data elaboration.

Figure 1. Absorbance FTIR spectra in the 2000-400 cm^{-1} range relative to neat BBS (green), neat magnetite M0 (black), and BBS-stabilized MB2 (red). The main relevant peaks are labeled. All spectra are collected in transmission mode through KBr pellets.

Figure 2. XRD patterns of the neat magnetite (M0) and BBS-stabilized sample (MB2). The main reflections due to magnetite are highlighted and labeled. Black symbol refers to the ammonium chloride phase (by-product).

Figure 3. Panel A: SEM micrograph of MB2 sample collected at 50000× magnification. Panel B: MB2 nanoparticles size distribution expressed as number of nanoparticles percentage (N/N_0%, where N_0 is the total of nanoparticles considered, i.e. 500).

Figure 4. Magnetization curves evaluation of neat magnetite and BBS-stabilized samples. Legend: M0 (black), MB1 (green), MB2 (red), and MB3 (blue). Inset shows the magnetic response of the BBS-stabilized materials vs. a commercially available neodymium magnet.

Figure 5. Panel A, TGA (solid line) and the derivative (dotted line) curves of the neat BBS (black) and MB2 (red) heated from 30 to 900°C at 10°C min^{-1} under dynamic nitrogen atmosphere. Panel B, FTIR profiles of the volatile CO_2 and NH_3 products released from neat BBS (black) and MB2 (red) during the heating ramp expressed as a function of temperature. Each curve represents the concentration (expressed as ppm/mg of sample) of the species evolved and it is obtained relating the IR absorbance at a specific wavenumber to the concentration by the Lambert-Beer's law relationship: CO_2 (2359 cm^{-1}), and NH_3 (965 cm^{-1}).

Figure 6. Fenton- and photo-Fenton-induced degradation of caffeine. Initial conditions: 5 mg L^{-1} caffeine, 0.4 mM H_2O_2, eventually 0.5 g L^{-1} magnetic-NPs or 0.001 g L^{-1} Fe(II), and UV irradiation (photo-Fenton). Panel A) Relative concentration of caffeine as a function of the irradiation time in photo-Fenton conditions. Legend: Photo-stability of caffeine under irradiation in presence of only H_2O_2 (white stars, grey dotted line), and degradation induced in presence of M0 (black squares, black solid line), MB1 (blue triangles, blue solid line), MB2 (red triangles, red solid line), and MB3 (green triangles, green solid line). Panel B) Photo-stability of caffeine under UV irradiation in presence of both H_2O_2 and BBS in homogeneous phase (green diamonds, green solid line), and photo-stability of caffeine under UV irradiation in presence of MB2, but in absence of H_2O_2 (brown circles, brown solid line). Panel C) Absorbance UV-Vis spectra in the 200-400 nm range relative to the caffeine solution before (black solid line) and after (grey solid line) degradation in presence of MB2/H_2O_2/UV (i.e. photo-Fenton) collected after 60 min of irradiation. The peak at 275 nm indicates the caffeine reference signal. Panel D) Fenton vs. photo-Fenton: Relative concentration of caffeine as a function of the (irradiation) time in Fenton/photo-Fenton conditions. Legend: Degradation of caffeine in presence of Fe(II) in Fenton (white diamonds, blue solid line) and photo-Fenton (blue diamonds, blue solid line), vs. MB2 in Fenton (white triangles, red solid line) and photo-Fenton (red triangles, red solid line) conditions.

Table 1. BET surface areas, BJH pore volumes and magnetite NPs size estimated by Scherrer equation applied on the XRD (311) magnetite main reflection.

Samples	BET surface area (m^2g^{-1})	BJH pore volume (cm^3g^{-1})	NPs mean size (nm)[a)]
M0	77	0.24	18 ± 3
MB1	4	0.03	27 ± 4
MB2	16	0.08	22 ± 6
MB3	33	0.06	16 ± 1

[a)] Calculated by substituting in **Equation 1** the line broadening at half the maximum intensity of the (311) magnetite reflection peak. Two different measurements are performed and average values are calculated. Diameters are reported in nm ± standard deviation.

Table 2. Evolved volatile species measured by TGA-FTIR analysis and data elaboration.

Samples	**Evolved volatile species measured by TGA-FTIR analysis**			**Composition (wt.%)**				
	Wt. (mg)	**$[CO_2]$[a)]**	**$[NH_3]$[b)]**	**BBS**	**Ashes**	**NH_4^+-salts**	**Fe_3O_4**	**BBS/Fe_3O_4 ratio**
BBS	22.757	753.511	398.289	68.8	31.2	---	---	---
$NH_4H_2PO_4$	31.823	---	4244.004	---	---	100.0	---	---
MB1	21.329	352.934	187.249	34.4	15.6	0.0	50.0	0.7
MB2	44.953	380.574	414.590	17.6	8.0	3.6	70.9	0.2
MB3	46.674	120.823	903.055	5.4	2.4	13.5	78.7	0.1

[a)]Calculated by integrating the CO_2 profile in the range of temperature 200-600°C (expressed as ppm/mg of sample); [b)]Calculated by integrating the NH_3 profile in the range of temperature 150-800°C (expressed as ppm/mg of sample).

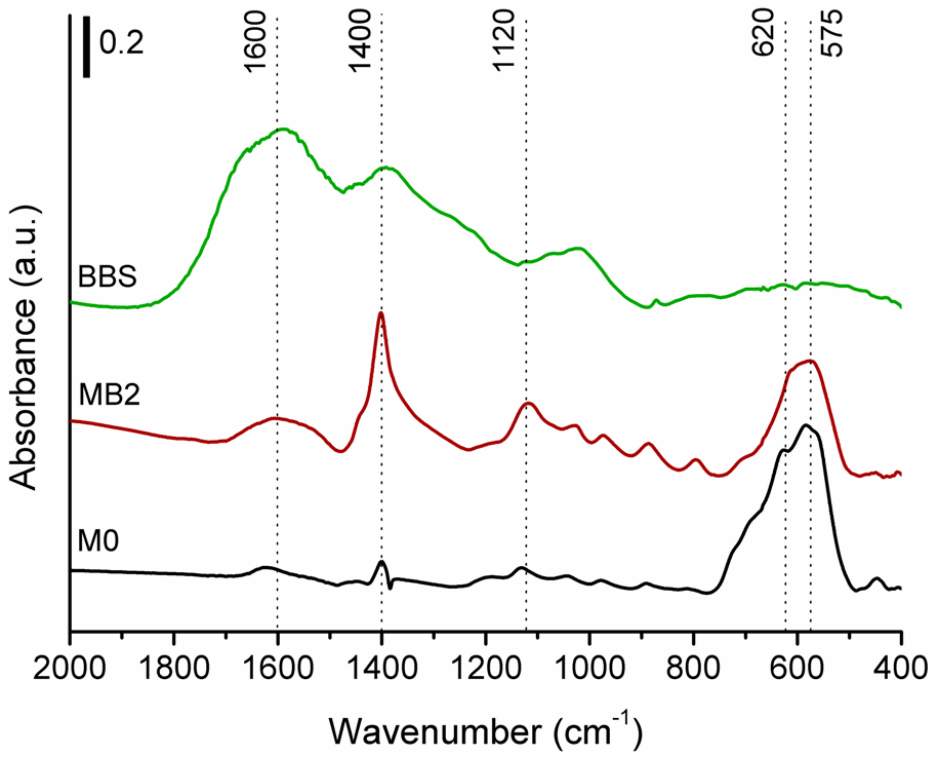

Figure 1. Absorbance FTIR spectra in the 2000-400 cm^{-1} range relative to neat BBS (green), neat magnetite M0 (black), and BBS-stabilized MB2 (red). The main relevant peaks are labeled. All spectra are collected in transmission mode through KBr pellets.

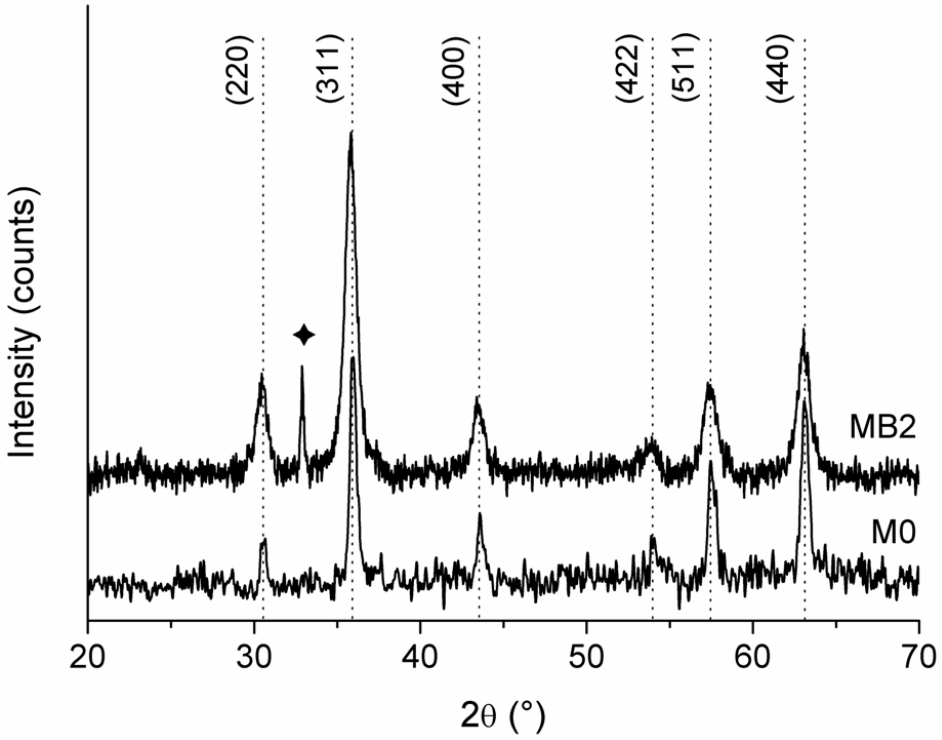

Figure 2. XRD patterns of the neat magnetite (M0) and BBS-stabilized sample (MB2). The main reflections due to magnetite are highlighted and labeled. Black symbol refers to the ammonium chloride phase (by-product).

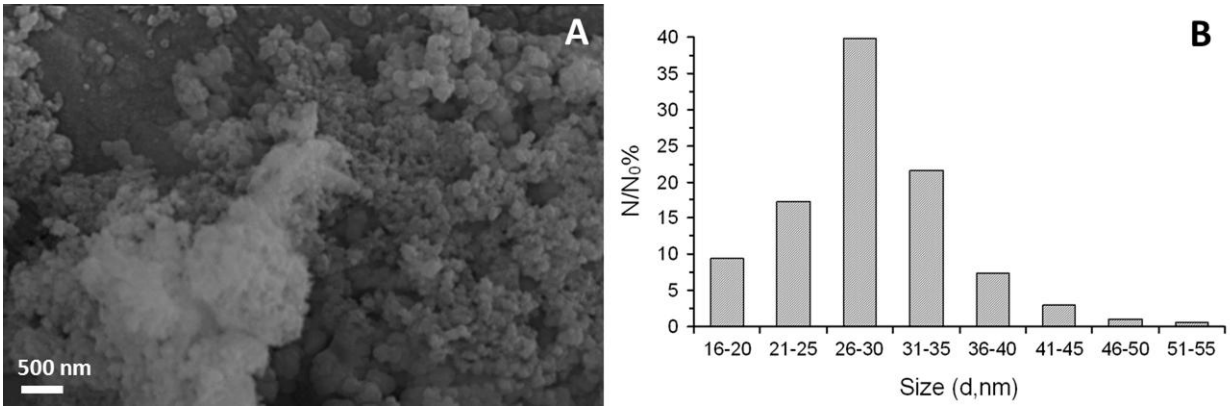

Figure 3. Panel A: SEM micrograph of MB2 sample collected at 50000× magnification. Panel B: MB2 nanoparticles size distribution expressed as number of nanoparticles percentage (N/N_0%, where N_0 is the total of nanoparticles considered, i.e. 500).

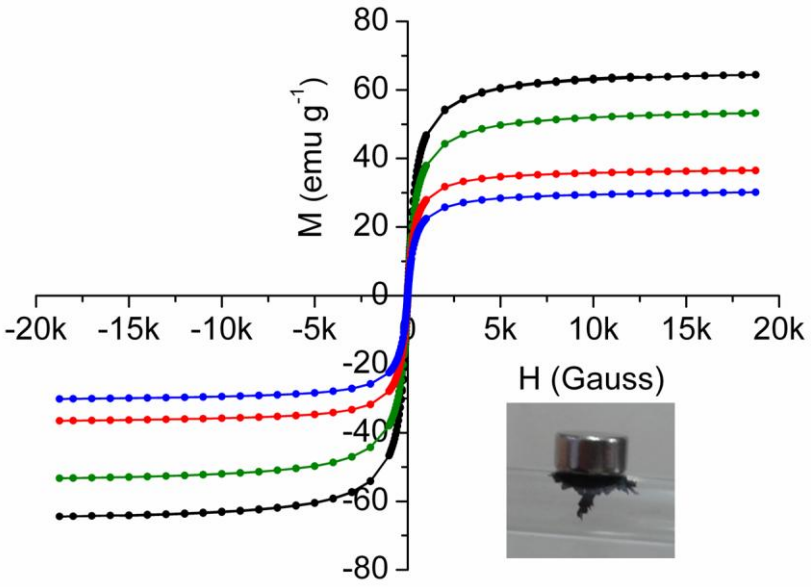

Figure 4. Magnetization curves evaluation of neat magnetite and BBS-stabilized samples. Legend: M0 (black), MB1 (green), MB2 (red), and MB3 (blue). Inset shows the magnetic response of the BBS-stabilized materials vs. a commercially available neodymium magnet.

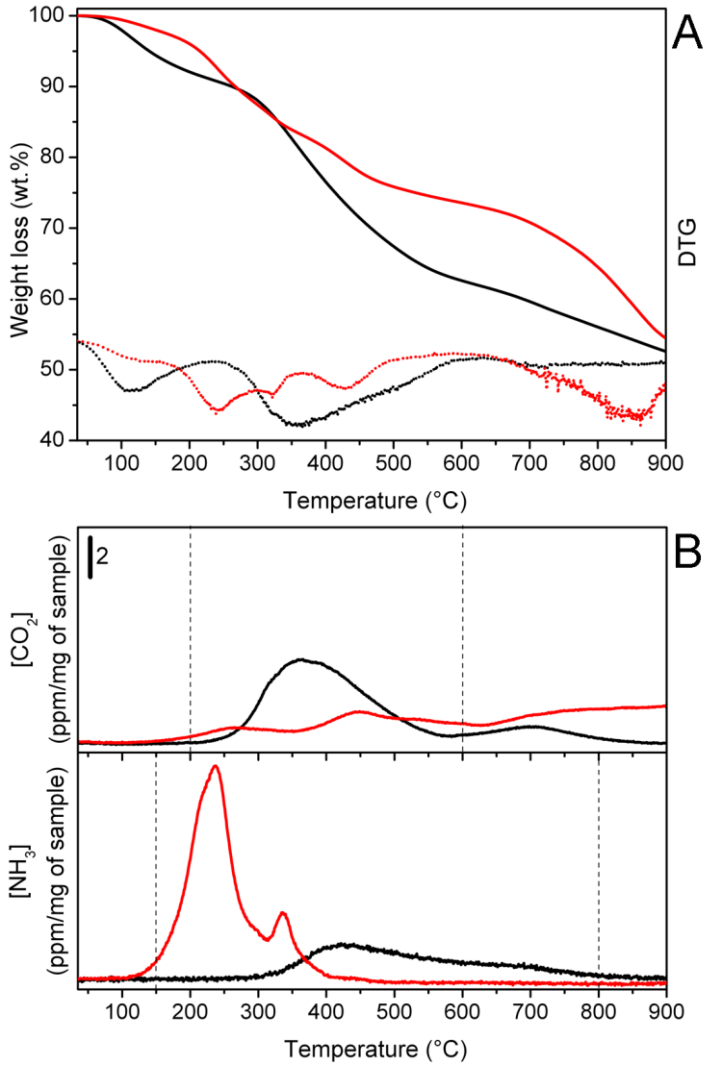

Figure 5. Panel A, TGA (solid line) and the derivative (dotted line) curves of the neat BBS (black) and MB2 (red) heated from 30 to 900°C at 10°C min^{-1} under dynamic nitrogen atmosphere. Panel B, FTIR profiles of the volatile CO_2 and NH_3 products released from neat BBS (black) and MB2 (red) during the heating ramp expressed as a function of temperature. Each curve represents the concentration (expressed as ppm/mg of sample) of the species evolved and it is obtained relating the IR absorbance at a specific wavenumber to the concentration by the Lambert-Beer's law relationship: CO_2 (2359 cm^{-1}), and NH_3 (965 cm^{-1}).

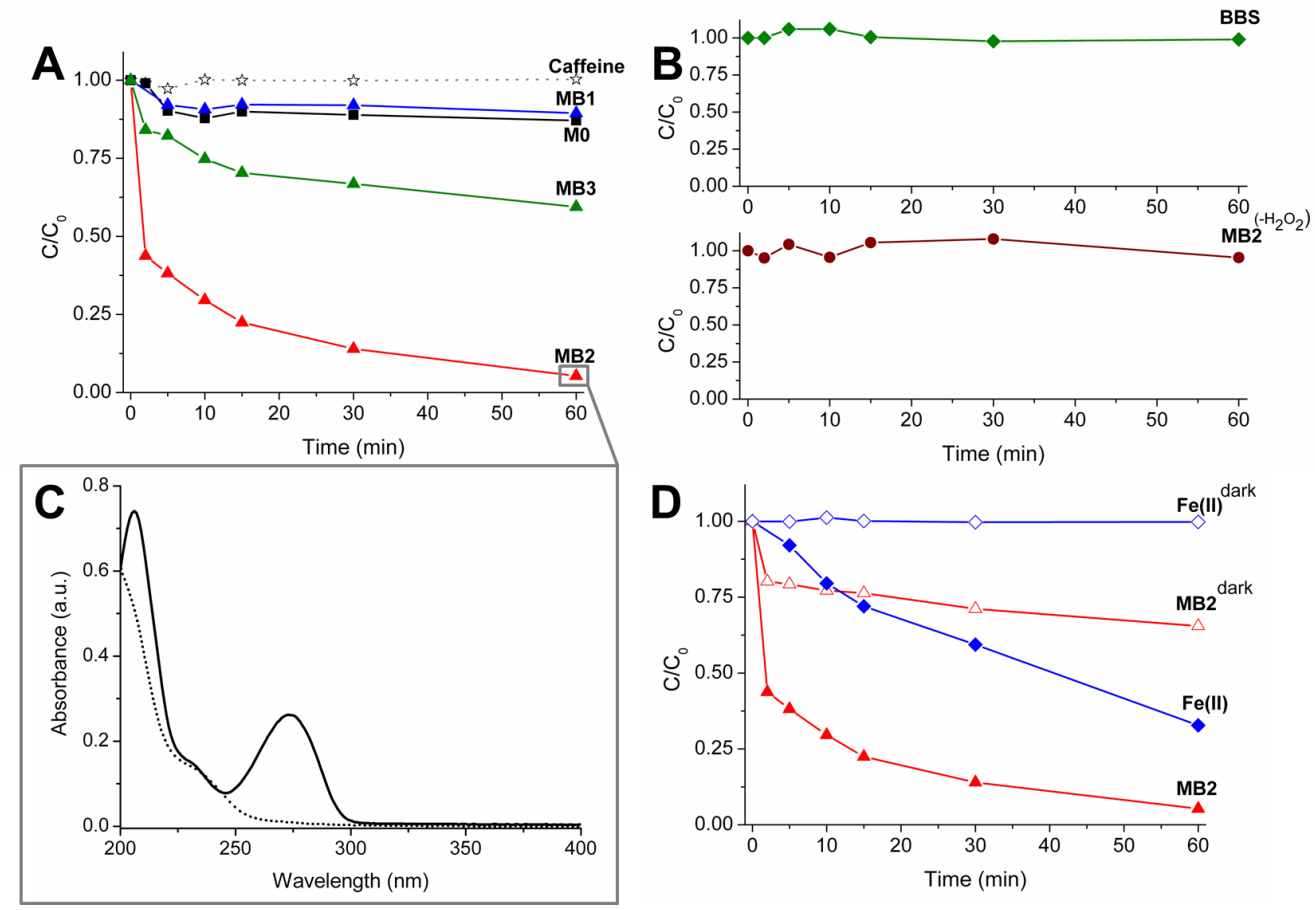

Figure 6. Fenton- and photo-Fenton-induced degradation of caffeine. Initial conditions: 5 mg L^{-1} caffeine, 0.4 mM H_2O_2, eventually 0.5 g L^{-1} magnetic-NPs or 0.001 g L^{-1} Fe(II), and UV irradiation (photo-Fenton). Panel A) Relative concentration of caffeine as a function of the irradiation time in photo-Fenton conditions. Legend: Photo-stability of caffeine under irradiation in presence of only H_2O_2 (white stars, grey dotted line), and degradation induced in presence of M0 (black squares, black solid line), MB1 (blue triangles, blue solid line), MB2 (red triangles, red solid line), and MB3 (green triangles, green solid line). Panel B) Photo-stability of caffeine under UV irradiation in presence of both H_2O_2 and BBS in homogeneous phase (green diamonds, green solid line), and photo-stability of caffeine under UV irradiation in presence of MB2, but in absence of H_2O_2 (brown circles, brown solid line). Panel C) Absorbance UV-Vis spectra in the 200-400 nm range relative to the caffeine solution before (black solid line) and after (grey solid line) degradation in presence of MB2/H_2O_2/UV (i.e. photo-Fenton) collected after 60 min of irradiation. The peak at 275 nm

indicates the caffeine reference signal. Panel D) Fenton vs. photo-Fenton: Relative concentration of caffeine as a function of the (irradiation) time in Fenton/photo-Fenton conditions. Legend: Degradation of caffeine in presence of Fe(II) in Fenton (white diamonds, blue solid line) and photo-Fenton (blue diamonds, blue solid line), vs. MB2 in Fenton (white triangles, red solid line) and photo-Fenton (red triangles, red solid line) conditions.